

RESEARCH

Open Access



# Biogenic surfactant mediated facile synthesis of visible light sensitized Zn/Mg co-doped TiO<sub>2</sub> nanomaterials – a green approach: evaluation of photocatalytic activity by degradation of Amido Black 10B

Genji Jaishree, Gorli Divya, Tirukkovalluri Siva Rao\*, M. L. V. Prasanna Chippada and Imandi Manga Raju

## Abstract

Visible light-driven Zn and Mg co-doped TiO<sub>2</sub> nanomaterials were synthesized by varying dopant concentrations in presence of biogenic surfactant *Sapindus emarginatus* (biogenic extract) via the Sol-gel method and have been successfully applied to the degradation of Amido Black 10B (AB 10B), an exemplary anionic textile azo dye pollutant. This study explored the potent capping properties of biogenic extract surfactant by encapsulating the Zn/Mg co-doped TiO<sub>2</sub>. In a view to assessing the physical and optical properties of the as-synthesized catalysts, various advanced instrumental techniques were adopted. The Transmission Electron Microscopy and Scanning Electron Microscopy analysis show the formation of small particle sizes (6.9 nm) pertaining to biogenic surfactant-assisted Zn/Mg co-doped TiO<sub>2</sub> (ZMT4S2). The substitutional doping of Zn and Mg into the TiO<sub>2</sub> framework by substituting Ti<sup>4+</sup> ion and the encapsulation of surfactant around catalyst was confirmed by Fourier Transform-Infrared Spectroscopy (FTIR) spectral studies. The surface area of the ZMT4S2 was found to be high (195 m<sup>2</sup>g<sup>-1</sup>) as compared with undoped TiO<sub>2</sub> (74 m<sup>2</sup>g<sup>-1</sup>) and Zn (1.00 wt%) / Mg (0.25 wt%) co-doped TiO<sub>2</sub> (ZMT4) (132 m<sup>2</sup>g<sup>-1</sup>). The red shift in the absorbance was observed for all the catalysts analyzed using UV-Vis-Diffuse Reflectance Spectroscopy (UV-Vis-DRS) confirms the ZMT4S2 showing less band gap of 2.1 eV than other catalysts. Further the electrical property of the catalyst was studied using Electrochemical Impedance Spectroscopy. The results obtained from impedance and Mott-Schotky plots show the reduced electrical resistance and electron hole recombination respectively. The sensitivity of the catalyst towards visible light was confirmed by its band gap energy measurement using UV-Vis-DRS. The anatase phase of all the catalysts was confirmed using powder X-ray diffraction. The composition and wt% of dopants revealed the Energy Dispersive X-ray spectra agree well with the calculated value. The slightly shifted frequency bands (FTIR) further confirmed the doping of Zn and Mg. The characterization analysis reports further accounts for the effective degradation of AB 10B dye (99%) taking place within 20 min of irradiation time at optimized reaction parameters such as best dopant concentration ZMT4, catalyst dosage (100 mg L<sup>-1</sup>), dye concentration (10 mg L<sup>-1</sup>) and solution pH 3.

**Keywords:** Zn/Mg-znO<sub>2</sub>, *Sapindus emarginatus*, Biogenic extract, Amido black 10B, Visible light Photodegradation

\*Correspondence: [sivaraoau@gmail.com](mailto:sivaraoau@gmail.com)

Department of Inorganic and Analytical Chemistry, Andhra University,  
Visakhapatnam 530003, India



© The Author(s) 2022. **Open Access** This article is licensed under a Creative Commons Attribution 4.0 International License, which permits use, sharing, adaptation, distribution and reproduction in any medium or format, as long as you give appropriate credit to the original author(s) and the source, provide a link to the Creative Commons licence, and indicate if changes were made. The images or other third party material in this article are included in the article's Creative Commons licence, unless indicated otherwise in a credit line to the material. If material is not included in the article's Creative Commons licence and your intended use is not permitted by statutory regulation or exceeds the permitted use, you will need to obtain permission directly from the copyright holder. To view a copy of this licence, visit <http://creativecommons.org/licenses/by/4.0/>.

## 1 Introduction

The benchmark photocatalyst, titanium dioxide ( $\text{TiO}_2$ ) in anatase form has been endorsed for its suitability for photocatalytic processes for effective removal of textile dye pollutants in an aqueous medium due to its strong oxidizing power, long-term stability, non-photocorrosive nature, etc. [1]. Even after rectifying the bandgap and electron-hole recombination of  $\text{TiO}_2$  by co-doping with metal/nonmetal or metal/metal [2], the rate of photocatalytic activity of the catalyst is still not satisfactory. To insight into this problem, many researchers have designed various methods to make a specific modification in  $\text{TiO}_2$  to reduce the band gap, electron-hole recombination [2], and increase the surface area [3] by applying different combinations of dopants and capping agent respectively.

Zhuang et al. worked on the synthesis of Sn and N co-doped  $\text{TiO}_2$  via sol-gel method through a post-nitridation route at  $500^\circ\text{C}$  for 20h [4]. Nasir et al. synthesized Ce/N co-doped  $\text{TiO}_2$  by hydrothermal method at  $120^\circ\text{C}$  precalcination treatment for 16h [5]. Mulpuri et al. reported the synthesis of Zn and B-codoped  $\text{TiO}_2$  by sol-gel method and found it effective for Acid Red degradation [6]. Although nonmetal doping of  $\text{TiO}_2$  can cause a red shift of  $\text{TiO}_2$  making it responsive to visible light, however during the annealing process, doped nonmetal content decreases [7] and as a result, the oxidizing ability of the  $\text{TiO}_2$  nanocrystalline phase is diminished in turn leading to decrement in photocatalytic activity.

Based on the above facts, various research groups have attempted different combinations of metals doped into  $\text{TiO}_2$  under visible light irradiation. Bakhshayesh et al. studied solar cell applications by using Sr and V co-doped  $\text{TiO}_2$  nanomaterials due to the easy incorporation of co-dopants into  $\text{TiO}_2$  lattice causing grain strain resulting in smaller crystallite size and inhibiting the growth of rutile phase which are advantageous for solar cell application [8].

Zn is found to be a promising potential photocatalytic promoter based on some of its merits such as the ionic radii of  $\text{Zn}^{2+}$  ( $0.74 \text{ \AA}$ ) and  $\text{Ti}^{4+}$  ( $0.75 \text{ \AA}$ ) are almost close to each other so a more effective substitution of  $\text{Ti}^{4+}$  ion with  $\text{Zn}^{2+}$  without disturbing the crystal structure, hence stabilizing the anatase phase [6]. Secondly, with Zn doping, the separation rate of the charge carriers was prolonged because of the introduction of an energy band just below the conduction band of  $\text{TiO}_2$  [9]. Er and Mg co-doped  $\text{TiO}_2$  catalysts were synthesized by Chen et al. via facile hydrothermal synthesis and applied for photovoltaic property in perovskite solar cell [10]. Among all the alkali earth metals  $\text{Mg}^{2+}$  has proven to be a landmark dopant due to its ionic radius ( $0.72 \text{ \AA}$ ) similar to that of  $\text{Ti}^{4+}$  [11]. Another

expedient role of Mg containing  $\text{TiO}_2$  is in reducing the band gap by forming an extra energy level just above the valency band by overlapping of 2p orbital of  $\text{Mg}^{2+}$  and  $\text{O}^{2-}$  [12]. Based on the importance and involvement of Zn and Mg as an individual dopants doped into  $\text{TiO}_2$  lattice, the present investigation proposed to synthesize Zn and Mg co-doped  $\text{TiO}_2$  by sol-gel method to take both the advantages of Zn and Mg. Moreover, Zn is an assuring n-type transition metal and it adsorbs organic pollutants like azo dyes [13]. In addition, Mg being electropositive favors the formation of a less dense anatase phase and shift the adsorption of radiation towards the visible region [14].

However, the enhanced surface area of a catalyst is a major contributing factor to effective photocatalytic activity. In the recent past, there are many capping agents assisting doped  $\text{TiO}_2$  synthesis process were studied [15]. Due to the rising concern regarding the biodegradability and long-term toxicity of synthetic surfactants. There is an urgency to develop an alternative green synthesis approach through biocapping as an ideal supplement [16] to reduce the particle size.

By considering the above-said facts, the present study attempted to use natural biogenic extract (*Sapindus emarginatus*) as a capping agent in the synthesis of Zn and Mg co-doped  $\text{TiO}_2$ . *S. emarginatus* (Soapnut) pericarp extract acts as a natural capping agent due to its major component saponin (Fig. 1) which in turn acts as a stabilizer and inhibits the agglomeration of doped  $\text{TiO}_2$  to nano size [17]. Balakrishnan et al. demonstrated good emulsification and low critical micellar concentration owing to its potent biodegradable surfactant properties. In addition to saponins, the presence of phytochemicals such as flavonoids, glycosides, fatty acids, and fixed oils makes it easier to use as a biocapping agent [18].

Recently great attention has been emphasized on the effective degradation of azo dyes which constitute about 60-70% of all the textile and industrial dyes together. Due to unique adverse toxic, mutagenic, and carcinogenic properties, these azo dyes have created a threat to the entire aquatic biota [19]. The present investigation envisages the visible light activity and catalytic efficiency of the synthesized catalyst evaluated by degradation of Amido Black 10B (AB 10B) dye as an exemplary pollutant. AB 10B is a classical azo dye consisting of sulphonic side chains ( $\text{C}_{22}\text{H}_{14}\text{N}_6\text{Na}_2\text{O}_9\text{S}_2$ ; see Fig. S1 of Supplementary material). Gokakakar et al. noticed that the presence of these sulfonic groups makes it easily soluble and stable, and becomes difficult to degrade by various conventional methods [20]. So herein, the as-synthesized Zn/Mg co-doped  $\text{TiO}_2$  was successfully employed for degradation of AB 10B to corroborate its effective photocatalytic efficiency.

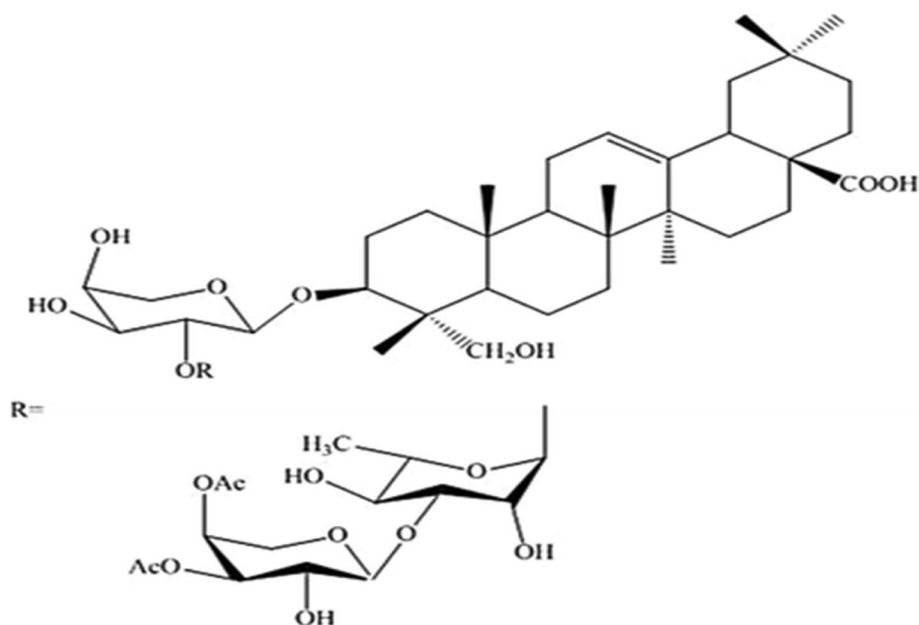


**Fig. 1** Structure of *Sapindus emarginatus* (Triterpenoid Saponin)

## 2 Experiment

### 2.1 Required chemicals and reagents

The main precursors of Titanium, Zinc, and Magnesium,  $\text{Ti}(\text{OBU})_4$  (98.6%),  $\text{Zn}(\text{NO}_3)_2 \cdot 6\text{H}_2\text{O}$  (99%), and  $\text{Mg}(\text{NO}_3)_2 \cdot 6\text{H}_2\text{O}$  (99.5%) respectively were used for the synthesis of undoped and Zn/Mg co-doped  $\text{TiO}_2$  catalysts. All the chemicals obtained were AR-Grade from E-Merck (Germany). AB 10B (90%) High Media, India was used as a model dye pollutant. *S. emarginatus* (soapnut) extract was used as the biogenic surfactant for the synthesis of Zn and Mg co-doped  $\text{TiO}_2$  (with surfactant). Ethanol and nitric acid are obtained from E-Merck (India) and used as a solvent in the reaction procedure. All the above-mentioned chemicals were used as received and their solutions were freshly prepared using deionized water.

### 2.2 Extraction of soapnut pericarp

The fresh ripen fruit of soapnut was taken, shade dried, and washed with deionized water, and then 100 g of pericarp soaked in 100 mL of water for 6 h. Then the clear solution was filtered using Whatman filter paper No. 1 and the 10 mL aliquot diluted to 100 mL (10%) was taken for further experimentation procedure.

### 2.3 Synthesis of Zn/Mg co-doped $\text{TiO}_2$

The synthesis of co-doped  $\text{TiO}_2$  catalysts were carried out using various weight percentages of dopants (Zn and Mg) by the sol-gel method. In beaker 1, n-Butyl ortho titanate (20 mL) was dissolved in absolute alcohol (40 mL) and stirred for 10 min, acidified with 3.2 mL of nitric acid

drop-wise under continuous stirring for 30 min (Solution I). In another Pyrex glass beaker 2, 40 mL of ethanol, the calculated (required weight percentage 0.25-1.0 wt%) amount of dopants, and 7.2 mL of water were taken and continued stirring for 30 min (Solution II). This was followed by the slow dropwise addition of Solution II (from burette) to Solution I, under vigorous stirring until the transparent sol was formed, and stirring was continued for 2 h. The sol formed is kept aside for 48 h for aging in dark at room temperature to obtain the gel. The gel was dried in an oven at 100 °C and ground. The catalyst powder was calcined at 450 °C in a muffle furnace for 5 h. The prepared catalysts were labeled as ZMT1, ZMT2, ZMT3, ZMT4, and ZMT5 as described in Table 1.

To select the best catalyst from the above-prepared catalysts, assessment studies were conducted for photocatalytic degradation of AB 10B dye under visible light irradiation and the results suggested that the best dopant concentration was obtained for ZMT4 with Zn (1.00 wt%) and Mg (0.25 wt%). To further boost the photocatalytic performance of the ZMT4 catalyst, scissoring of the catalyst by using biogenic soapnut extract as capping agent to control the agglomeration of the particles for getting smaller particle sizes resulting in high surface area. Soapnut extract-assisted ZMT4 nanocatalysts were synthesized by following the same procedure but varied volumes (5, 10, and 15 mL) of soapnut 10% extract was added after the sol formation in the regular procedure and continued the stirring for 15 min left the solution for aging. A similar procedure was adopted for the synthesis

**Table 1** Details of all the samples synthesized

Weight percentages of dopants (wt%)	<i>Sapindus emarginatus</i> surfactant (Volume in mL)	Name assigned to the sample
NIL	–	UTO (Undoped TiO <sub>2</sub> )
0.25 Zn/0.75 Mg	–	ZMT1
0.50 Zn/0.50 Mg	–	ZMT2
0.75 Zn/0.25 Mg	–	ZMT3
1.00 Zn/0.25 Mg	–	ZMT4
1.00 Zn/0.50 Mg	–	ZMT5
1.00 Zn/0.25 Mg	5	ZMT4-S1
1.00 Zn/0.25 Mg	10	ZMT4-S2
1.00 Zn 0.25 Mg	15	ZMT4-S3

of undoped TiO<sub>2</sub> (without the addition of dopants and soapnut extract). Details of all the as-synthesized catalysts are presented in Table 1.

#### 2.4 Instrumental techniques utilized for characterization of the catalyst

Powder X-ray diffraction (XRD) measurements were accomplished to determine the crystalline phase of undoped TiO<sub>2</sub> and Zn/Mg co-doped TiO<sub>2</sub> in the presence and absence of a capping agent, using an X'PERT MPD\_PRO diffractometer (Malvern Panalytical, Malvern, United Kingdom) with Cu K $\alpha$  radiation operated at 45 kV, 40 mA and 0.2  $\theta$  scan rate ( $\lambda = 0.15405$  nm). The average crystallite size of anatase form was determined according to the Scherer equation using full width at half maximum of the diffraction peak data of the selected peak. Fourier-transform infrared (FTIR) spectra of the samples were recorded in a frequency ranging from 4000 to 400 cm<sup>-1</sup> using an FTIR spectrometer type JASCO 4100 (Jasco International, Tokyo, Japan) in transmission mode using the KBr pellet method. UV-Visible diffuse reflectance spectroscopy (UV-DRS) with Shimadzu 3600 UV-Vis DRS Spectrophotometry in the range of 200–800 nm with BaSO<sub>4</sub> taken as a reference to determine the band gap of as-synthesized catalysts. The morphology of the catalyst was studied using a scanning electron microscope (ZEISS SIGMA FE-SEM) equipped with an energy dispersive X-ray Spectrophotometer with a resolution 1 nm @ at 15 kV with high definition scan. The Elemental composition was identified using the X-ray Fluorescence (XRF) (XGT 5200, Horiba, Japan) with an X-ray tube 50 kV max, 1 mA with Rh target. The size and shape of the nanoparticles were recorded with TECNAI FE12 Transmitted Electron Microscopy (TEM), operated current was 120 kV. The pore volume ( $V_p$ ), size, and surface area ( $S_{BET}$ ) were determined by N<sub>2</sub> adsorption-desorption isotherm at 77.3 K using the instrument Brunauer-Emmett-Teller (BET) Quanta chrome Nova 2200 E

System. Photoluminescence measurements were performed using Hitachi F-7000 fluorescence spectrophotometer. UV-Vis spectrophotometer (Shimadzu 1601) was used to monitor the assays of AB 10B degradation during the photocatalysis process. Elico digital pH meter (Model III E, EI) was used to monitor the change in the pH of the solution during the degradation process.

To explore the electronic processes in undoped (UTO) and co-doped TiO<sub>2</sub> (ZMT4S2), the Electrochemical Impedance Spectroscopy (EIS) measurements were conducted under illumination conditions (using Gamry Potentiostat/Galvanostat, Interface 1010E), in a standard three-electrode system using the prepared samples as the working electrodes with an active area of 1 cm<sup>2</sup>. The samples for EIS measurements were prepared by spin-coating a thin layer of photocatalyst sample on (5 mg of sample dispersed in absolute 1-butyl alcohol) at the spin-coating speed of 3000 rpm for 30 s. After drying at 100 °C for 30 min the samples were further annealed at 200 °C for 1 h. The saturated calomel electrode (SCE) and platinum wire were used as reference and counter electrodes. The EIS measurements were done in the frequency range from 100 kHz to 100 MHz with the applied potential of 50 mV. The electrolytic solution used for the EIS experiment was 0.1 M KOH. The Mott-Schottky measurement was carried out at different frequencies 0.5, 1, and 1.5 kHz and fitted linearly to obtain flat band potential. All the analyses were done using Gamry Echem Analyst software.

#### 2.5 Experimental setup and evaluation procedure for photocatalytic activity

The photocatalytic activity of the Zn and Mg co-doped TiO<sub>2</sub> nanomaterial samples was evaluated by the degradation of AB 10B. As a visible light source, the high-pressure mercury metal halide lamp (Osram, India) 400 W was used as a visible light source output of 436–546 nm with 35,000 Lm with UV filter (Oriel no: 51472) to cut

off the UV radiation. The experimental setup is given in Fig. 2. The photocatalytic procedure was given as follows: In a 150 mL pyrex glass reaction vessel 100 mL of dye solution with preset concentrations (5, 10, 15 and  $20 \text{ mg L}^{-1}$ ) were taken and the catalyst dosages 0.05, 0.10, 0.15 and  $0.20 \text{ g } 100 \text{ mL}^{-1}$  were added to it and the solution pH was adjusted by the addition of either 0.1 N HCl or 0.1 N NaOH. Before illumination, the mixtures were magnetically stirred under dark for the establishment of adsorption/desorption equilibrium of AB 10B on the surface of the catalyst. To filter off IR radiation and to maintain the reaction condition at room temperature mixture was kept under running cool water which was circulated around the sample container. The rate of reaction was followed by withdrawing 5 mL aliquots of samples from the reaction mixture by using a millipore syringe ( $0.45 \mu\text{m}$ ) at different time increments and measuring the absorption of the sample at  $\lambda \text{ max } 619 \text{ nm}$  by using a UV-Vis spectrophotometer (Shimadzu 3600). The percentage of degradation of the dye (AB 10B) was calculated by using the following equation. % of degradation =  $(C_o - C_t) / C_o \times 100$ , where  $C_o$  is the initial absorbance of dye solution before exposure to light and  $C_t$  is the absorbance of dye solution at a time,  $t$  after exposure to light.

### 3 Results and discussion

#### 3.1 XRD

The powder XRD technique was utilized to analyze the structural properties of catalyst samples with and without surfactant (Fig. 3a and b). The  $2\theta$  values of each peak of all the catalysts were found at 25.3, 37.8, 47.9, 54.5, 57.1, and 62.5°, corresponding to (101), (004), (200), (105),

(211) and (204) crystal planes of  $\text{TiO}_2$  respectively, indicating the presence of anatase phase. The peaks almost coincide with undoped  $\text{TiO}_2$  depicting that the presence of dopants has no influence on the anatase phase of  $\text{TiO}_2$  calcined at  $450^\circ\text{C}$  for 5 h [21]. This may be due to the ionic radii of  $\text{Zn}^{2+}$  ( $0.74 \text{ \AA}$ ) and  $\text{Mg}^{2+}$  ( $0.72 \text{ \AA}$ ) is almost close to that of  $\text{Ti}^{4+}$  ( $0.75 \text{ \AA}$ ), hence more effective substitution of both the dopants into  $\text{TiO}_2$  lattice has occurred by substituting  $\text{Ti}^{4+}$  ions [6, 11]. This can be further evident from the fact that no peaks at  $2\theta = 31.7, 34.5, 36.3, 47.5, 56.2$  and  $62.7^\circ$  for ZnO and  $2\theta = 36.7, 42.7$  and  $62.0^\circ$  for MgO were observed [22, 23]. Further, it indicated that from Fig. 3b the presence of intense and sharp peaks for ZMT4S2BC attributed to the effective capping of co-doped  $\text{TiO}_2$  with biogenic surfactant [17]. Using the Debye Scherrer equation ( $d = k\lambda / \beta \cos\theta$ ) [15] average crystallite size of undoped, Zn/Mg codoped- $\text{TiO}_2$  and capped Zn/Mg codoped- $\text{TiO}_2$  were calculated and presented in Table 6. From Table 6 it can be inferred that the crystallite size for capped ZMT4S2 (5.7 nm) is lesser than undoped ZMT4 (7.0 nm).

#### 3.2 TEM

The particle size of the catalyst was analyzed by the TEM with the images shown in Fig. 4, describing the surface morphology and particle size distribution of undoped  $\text{TiO}_2$ , ZMT4, and ZMT4S2. Figure. 4a depicts the nanospheres agglomerated particles of undoped  $\text{TiO}_2$ . Clear nanospheres with small particle size and less agglomeration for ZMT4 (Fig. 4b) and no agglomeration for ZMT4S2 (Fig. 4c) were observed. From the Gaussian fitting method shown in the inset of Fig. 4b

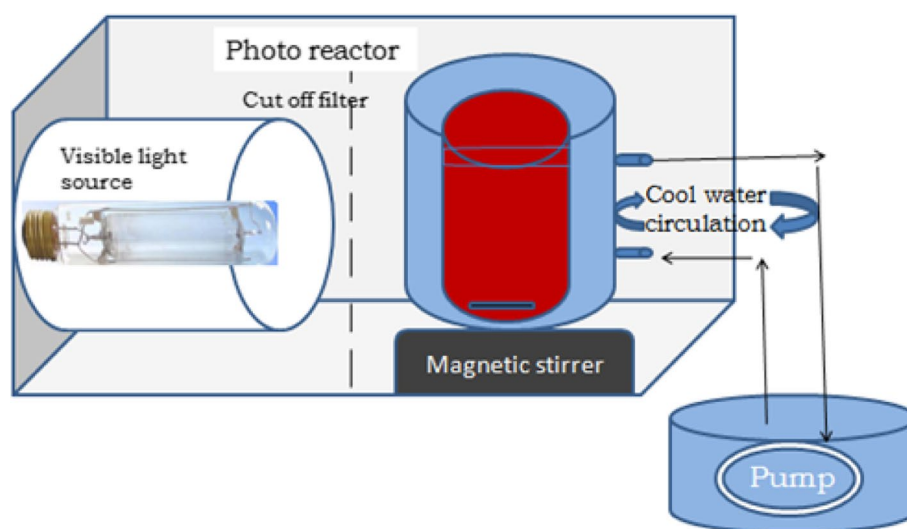
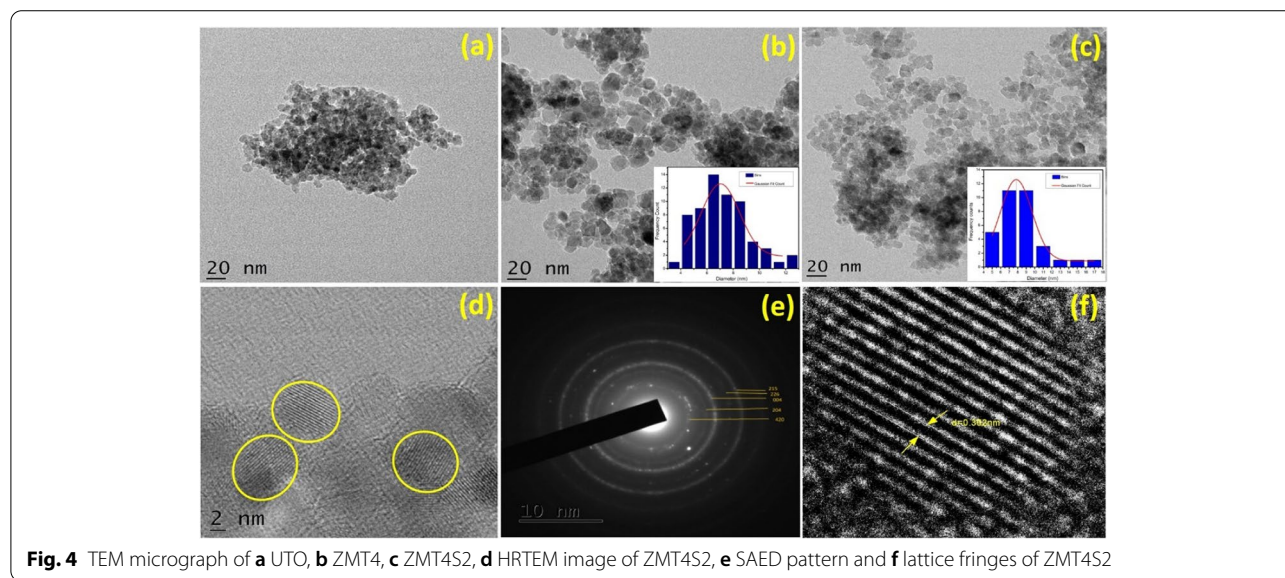
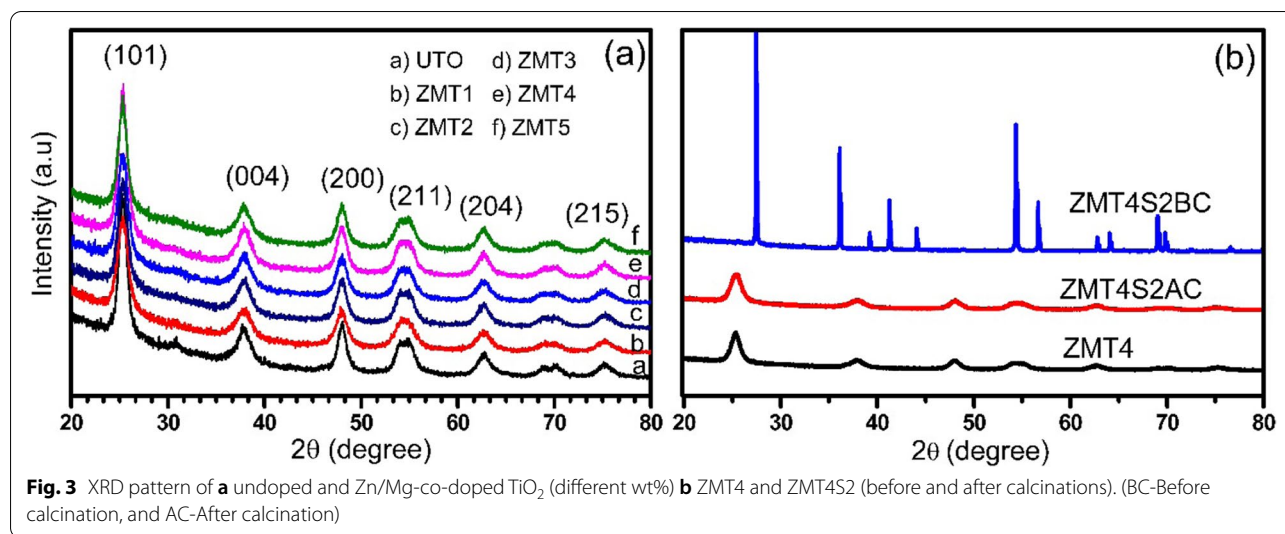


**Fig. 2** Schematic representation of photo reactor



and c. The particle size distribution histograms were obtained which indicated that the average particle size of ZMT4 and ZMT4S2 was found to be 7.8 and 6.9 nm respectively. The decrease in the particle size of ZMT4S2 is may be due to the encapsulation of biogenic surfactant (capping agent) during the synthesis process. The HRTEM image (Fig. 4d) exhibits that the ZMT4S2 contains randomly oriented nanocrystals with anatase phases. The SAED pattern of ZMT4S2 (Fig. 4e) was also studied for the concentric rings attributed to the polycrystalline nature as indicated by the (420), (204), (004), (226) and (215) anatase planes in good concordance with the XRD results. Moreover, the interplanar space

determined for a tetragonal structure anatase 101 peak was found to be 0.30 nm (Fig. 4f).

### 3.3 FTIR analysis

Figure 5 displayed the FTIR spectrum of undoped TiO<sub>2</sub>, ZMT4, and ZMT4S2BC. The spectra revealed the peak at 512 cm<sup>-1</sup>, attributed to the stretching vibration of Ti-O-Ti of undoped TiO<sub>2</sub> which has been shifted to 490 cm<sup>-1</sup> for all the doped samples implies the doping of Zn and Mg into TiO<sub>2</sub> framework by substituting Ti<sup>4+</sup> ion [24]. The peaks at 1633 cm<sup>-1</sup> related to H-O-H bending vibration, and the peaks at 3000 – 3400 cm<sup>-1</sup> correspond to the stretching vibration of the surface hydroxyl groups

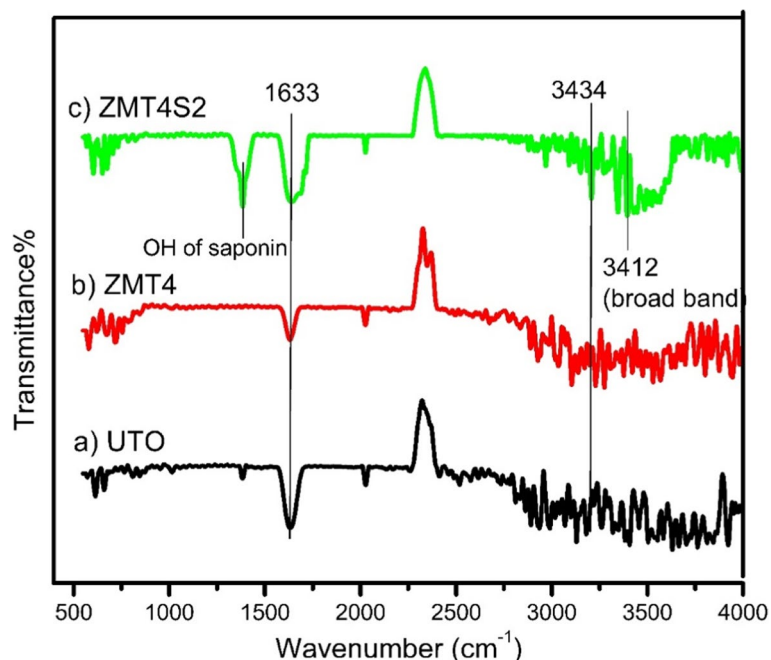


**Fig. 5** FTIR spectra of **a** UTO, **b** ZMT4 and **c** ZMT4S2BC

of O-H which is in good agreement with the literature reports [25]. No peaks were observed at  $457\text{ cm}^{-1}$  and broad peak in the range  $3300\text{--}3600\text{ cm}^{-1}$  indicated the absence of ZnO and MgO, which coincides with the XRD results [26, 27]. The stretching frequencies observed at  $1201$  and  $1065\text{ cm}^{-1}$  attributed to Zn-O-Ti and Mg-O-Ti which is evident for the substitutional doping of Zn and Mg by replacing  $\text{Ti}^{4+}$  ion in  $\text{TiO}_2$  lattice [6, 28]. In addition, the peaks corresponding to the stretching frequencies of Saponins (*S. emerginatus* pericarp) have been shifted when it encapsulated the catalyst particles. These results of saponins and flavonoids with respect to ZMT4S2 are presented in Table 2.

### 3.4 BET surface area analysis

Figure 6a and b explained the  $\text{N}_2$  adsorption–desorption isotherms and BJH pore size distribution curves of ZMT4 and ZMT4S2 calcined at  $450^\circ\text{C}$ , respectively. The bioextract has been explored for its potent capping properties and the plot exhibits a type IV isotherm with a type  $\text{H}_2$  hysteresis (according to the IUPAC classification) which suggests that the sample is mainly classified as mesoporous [29] with enhanced surface area ( $195\text{ m}^2\text{ g}^{-1}$ ) of ZMT4S2 when compared to ZMT4 ( $132\text{ m}^2\text{ g}^{-1}$ ). The difference in surface area may be contributed by the effective capping derived from ambipolar characteristics of triterpenoid (a major

**Table 2** Comparative stretching frequency values of pericarp extract and ZMT4S2BC

Compound prepared	Stretching frequencies to be measured for	Frequencies/ $\text{cm}^{-1}$	
		Frequency values for <i>Sapindus emerginatus</i> pericarp extract	Shifted frequency values for ZMT4S2BC (before calcination)
<i>Sapindus emerginatus</i> pericarp [25]	O–H stretching vibration of flavonoids	3407	3412 (broad band)
	carboxylic O–H bond stretching vibration of saponins	2875	2994
	carboxylic C=O bond stretching vibration of saponins	1618	1633
	C=O stretching vibration of flavonoids	1693	1764
	carboxylic O–H bending vibration of saponins	1050	1376

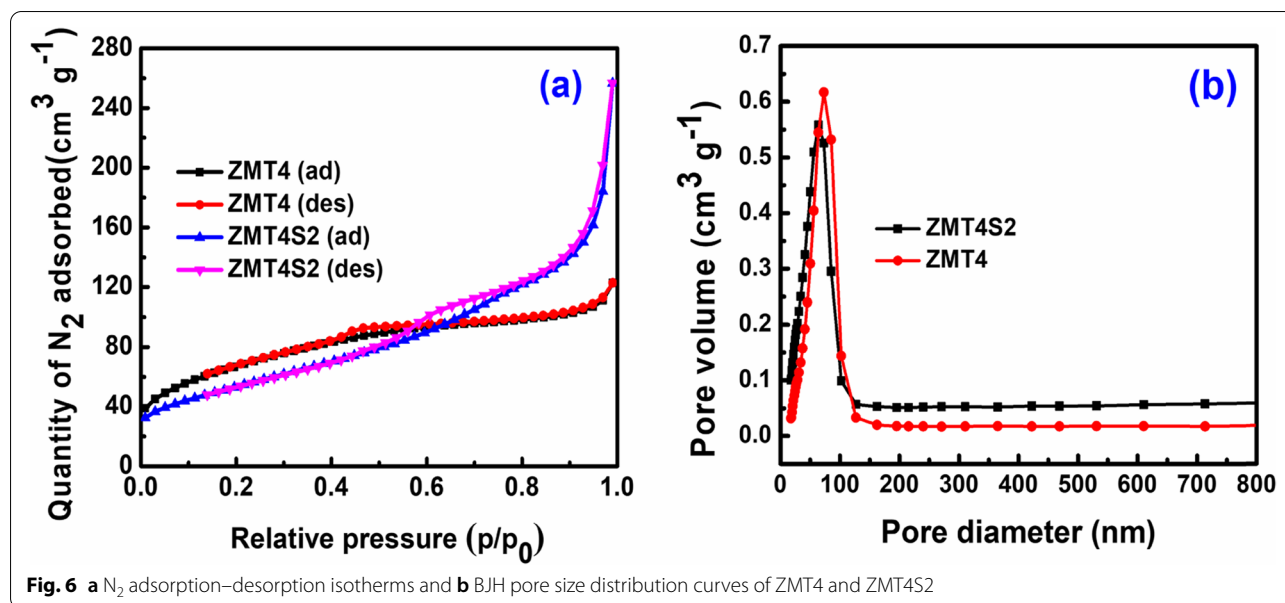


**Fig. 6** a  $N_2$  adsorption–desorption isotherms and b BJH pore size distribution curves of ZMT4 and ZMT4S2

component of saponin) which in turn accounts for non-agglomeration and stability of as-synthesized ZMT4 catalysts (in the presence of biogenic surfactant) [18]. The increase in the surface area follows the trend as  $ZMT4S2 > ZMT4S1 > ZMT4S3$  since saponin (of the biogenic extract) is a non-ionic surfactant and the presence of bulkier terpenoid molecule is capable of showing capping property up to optimized surfactant concentration. Beyond the optimum concentration, the degree of interaction of hydrophilic groups with the  $TiO_2$  lattice decreases due to more crowding which restricts the formation of micelles. Hence, an increase in critical micellar concentration decreases the encapsulation [30].

### 3.5 UV–vis-DRS

UV–Vis DRS spectra of synthesized Zn/Mg co-doped  $TiO_2$  around 400–500 nm showed a remarkable redshift in the wavelength as compared to undoped  $TiO_2$  (Fig. 7a). This shift may be resulted from the substitutional doping of  $TiO_2$  by Zn and Mg which was in turn caused by an extra energy level band formed above the valence band by replacing  $Ti^{4+}$  in  $TiO_2$  by  $Mg^{2+}$ . The mixing of Mg (2p) with O (2p) orbital facilitates electron excitement in the visible region [31]. In addition, the incorporation of  $Zn^{2+}$  contributes to the prolonged separation of charge carriers [9]. Further, it was supported by the calculated band gap energies of all synthesized catalysts using the Kubelka-Monk formalism plot and Tauc's plot method as shown in Fig. 7b. The undoped  $TiO_2$  exhibited a band gap of 3.12 eV but the co-doped  $TiO_2$  samples showed a band gap ranging from 2.7 to 2.9 eV. Among all the co-doped samples ZMT4 exhibits the lowest band gap energy of

2.7 eV. The results indicate that co-doping of Zn and Mg made all the catalysts to be visible light active, by which a greater number of electron-hole pairs are generated by the absorption of visible light, leading to higher photocatalytic activity. Moreover, the addition of surfactant led to the further reduction in bandgap to 2.1 eV which suggests that oxygen deficiency displayed excellent sensitivity towards visible light and enhanced photocatalytic efficiency. The comparison results of the bandgap of singly doped and surfactant-assisted co-doped  $TiO_2$  are tabulated in Table 3.

### 3.6 EIS

The EIS study dealing with electrical mechanism of nanocatalyst using impedance is depicted in Fig. 8a and b. The complex impedance (Nyquist) plot for UTO and ZMT4S2 was well fitted with the equivalent circuit shown in the inset of Fig. 8a and b. The plot is almost a vertical line which may be attributed to constant phase element having its negligible contribution. The derived Warburg diffused impedance ( $Z_w$ ) might be due to low charge transfer resistance. The circuit parameter values are represented in Table 4, where  $R_s$  is the solution resistance and  $R_{CT}$  is the charge transfer resistance. It can be inferred from the results that  $R_s$  and  $R_{CT}$  values are low for ZMT4S2 than those of UTO. The capacitance  $C$  values were calculated using the simple relation:  $-Z'' = (j\omega C)^{-1}$ , where  $C$  is the capacitance,  $Z''$  is the imaginary part of the impedance function,  $\omega$  is the angular frequency ( $2\pi f$ ) and complex quantity ( $j$ ) =  $\sqrt{-1}$  [32]. The flat-band potential ( $E_{fb}$ ) can be obtained by the Mott-Schotky function using the capacitance value from the conduction band

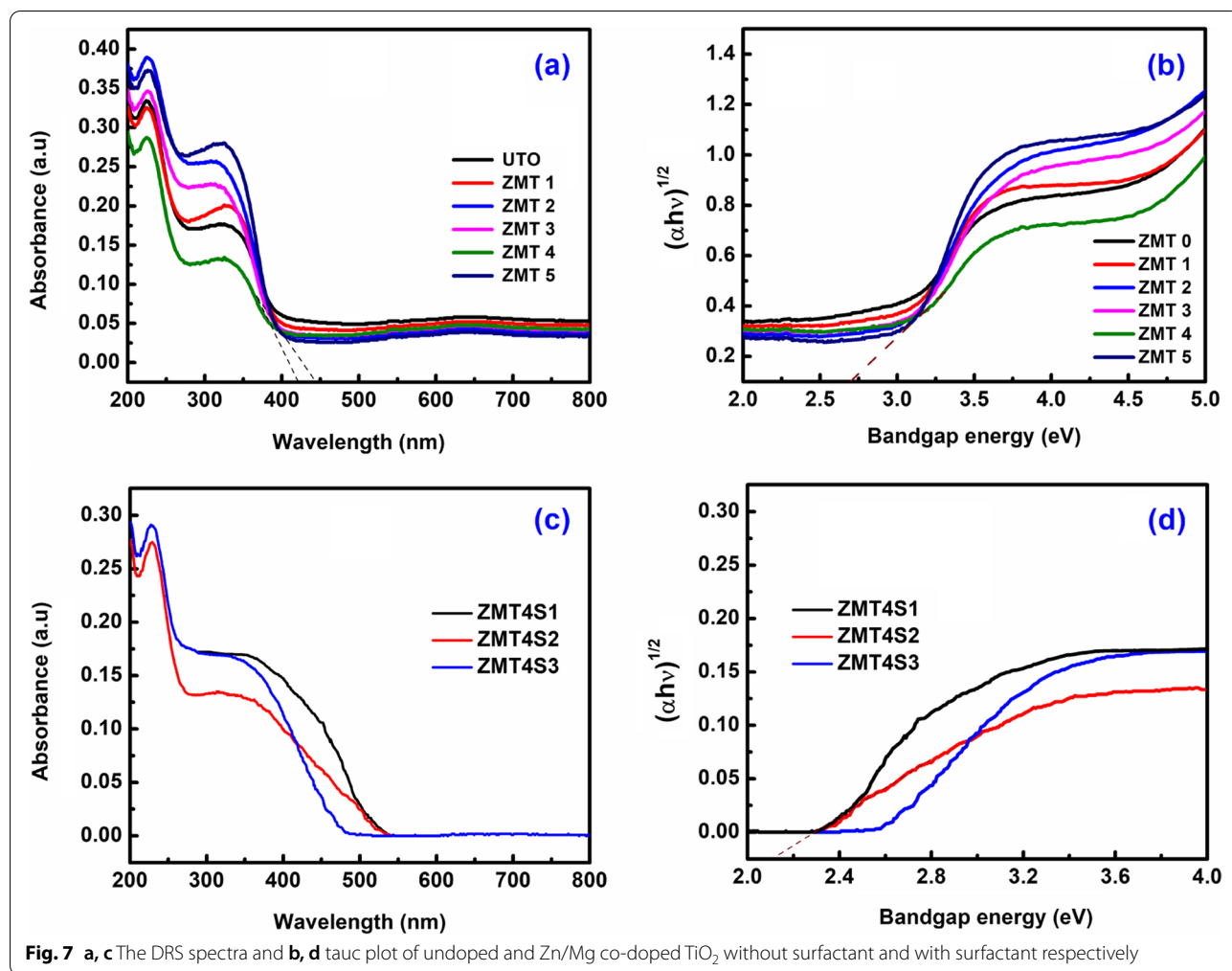


**Table 3** Comparative band gap values of Zn and Mg single doped, Zn/Mg co-doped TiO<sub>2</sub> and surfactant assisted Zn/Mg co-doped TiO<sub>2</sub>

Catalyst	Bandgap (eV)
Zn doped TiO <sub>2</sub> [9]	3.20
Mg doped TiO <sub>2</sub> [31]	2.87
Zn and Mg doped TiO <sub>2</sub> (Present work)	2.70
Surfactant assisted Zn and Mg codoped TiO <sub>2</sub> (Present work)	2.10

minimum (CBM), and the valence band maximum was estimated based on the difference from the CBM using the “optical bandgap energy” determined by the Tauc plot as presented in Fig. 8c and d, respectively. Both the Mott–Schotky plots show the positive slope indicative of the n-type semiconductor behavior of TiO<sub>2</sub>. In addition, the presence of Mg (0.25 wt%) has shown the positive shift in E<sub>fb</sub> (1.83) and reduced recombination, while doping

with Zn has shifted the E<sub>fb</sub> towards a more negative value (−0.17 eV) as compared to undoped TiO<sub>2</sub> (−0.058 eV) which was obtained by linearly fitting the plots measured at different frequencies (0.5, 1 and 1.5 kHz). This change is evidence for the increased electron densities and electron transport across interfaces [32].

**3.7 SEM–EDX and XRF analysis**

Figure 9 shows the SEM images of undoped and ZMT4 depicting the spherical shape and uneven distribution of particles size due to the doping Zn and Mg compared with undoped TiO<sub>2</sub>. Further, the presence of doped ions in the ZMT4 was confirmed by EDX. The EDX spectrum (Fig. 9d) reveals that the diffraction peaks corresponding to Zn at 1.00 and 8.75 keV and for Mg at 1.25 keV infer the presence of doped ions. The overall data show the atomic wt% of Zn and Mg which are in good concordance with the calculated value. The elemental composition of Zn/Mg co-doped TiO<sub>2</sub> was further evidenced from the XRF analysis as depicted

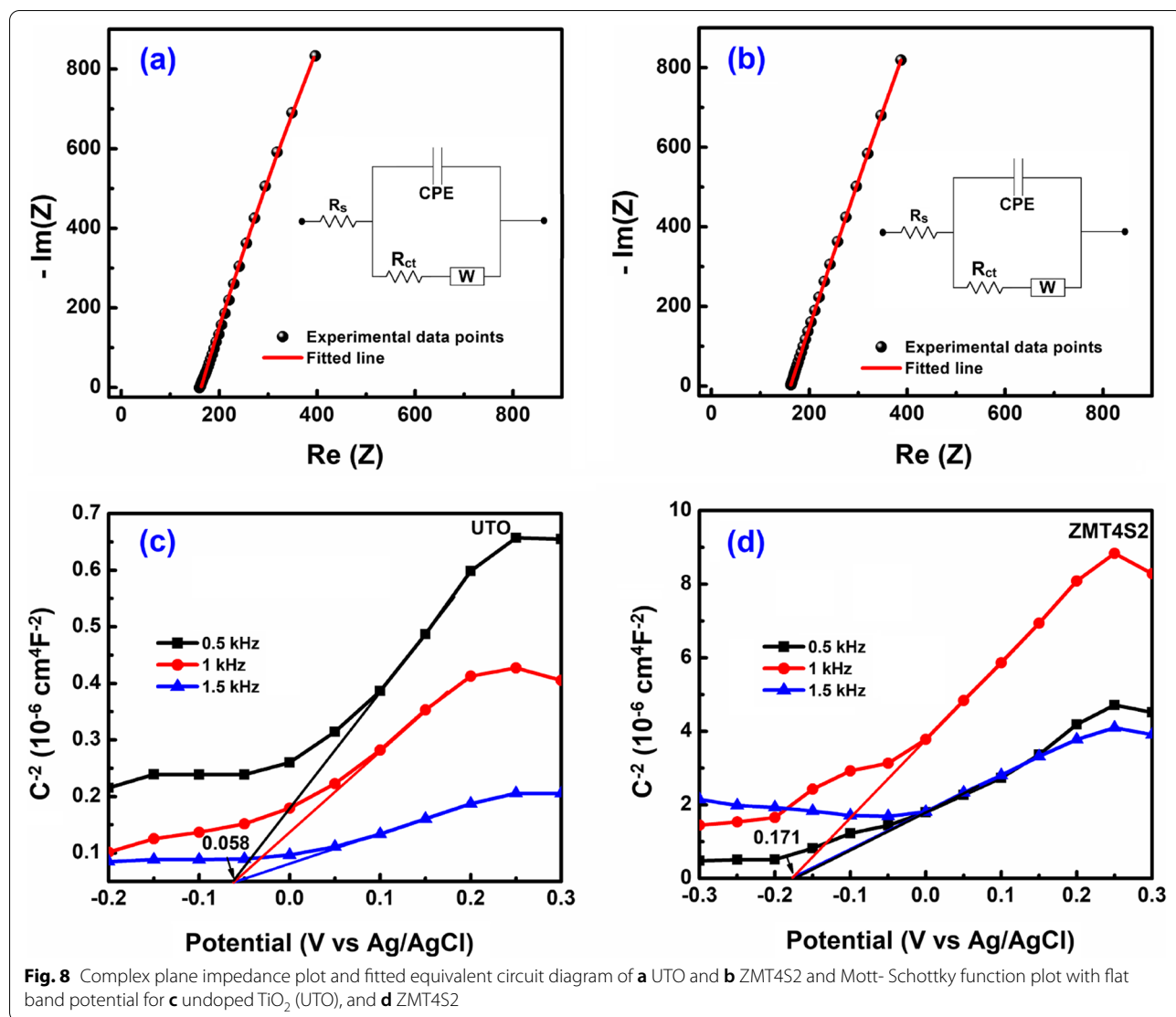


**Fig. 8** Complex plane impedance plot and fitted equivalent circuit diagram of **a** UTO and **b** ZMT4S2 and Mott-Schottky function plot with flat band potential for **c** undoped TiO<sub>2</sub> (UTO), and **d** ZMT4S2

in Table 5 with atomic wt% corresponding to Zn (1.07) and Mg (0.23) approximately coinciding with dopants wt% i.e. Zn (1.00) and Mg (0.25).

**4 Photocatalytic performance of ZMT4 and ZMT4S2 (after calcination)**

To explore the photo-degradability of AB 10B dye with ZMT4 and ZMT4S2 catalysts under visible light irradiation, a series of experiments were designed to determine the reaction conditions for better degradation of

**Table 4** EIS fitting parameter values of UTO and ZMT4S2

Parameters	UTO	ZMT4S2
R <sub>s</sub> (Ω)	163	95
R <sub>ct</sub> (kΩ)	35	2
C <sub>sc</sub> (F)	5.0 E <sup>-14</sup>	1.5 E <sup>-14</sup>

dye. Before establishing the reaction conditions, trial experiments were conducted to know the sensitivity of dye and catalyst toward visible light.

**4.1 Photolysis**

100 mL of 5 mgL<sup>-1</sup> AB 10B dye solution was added in a 150 mL pyrex glass vessel without catalyst and exposed to light for 60 min. 5 mL of aliquots were withdrawn at different time intervals and measured the absorbance at λ<sub>max</sub> of 619 nm. No appreciable change in the absorbance was observed for the dye solution before and after exposure to light implies that the insensitivity of dye towards the light.

**4.2 Adsorption**

The reaction vessel containing dye solution (5 mgL<sup>-1</sup>) with catalyst dosage (0.05 g 100 mL<sup>-1</sup>) at pH=3 was

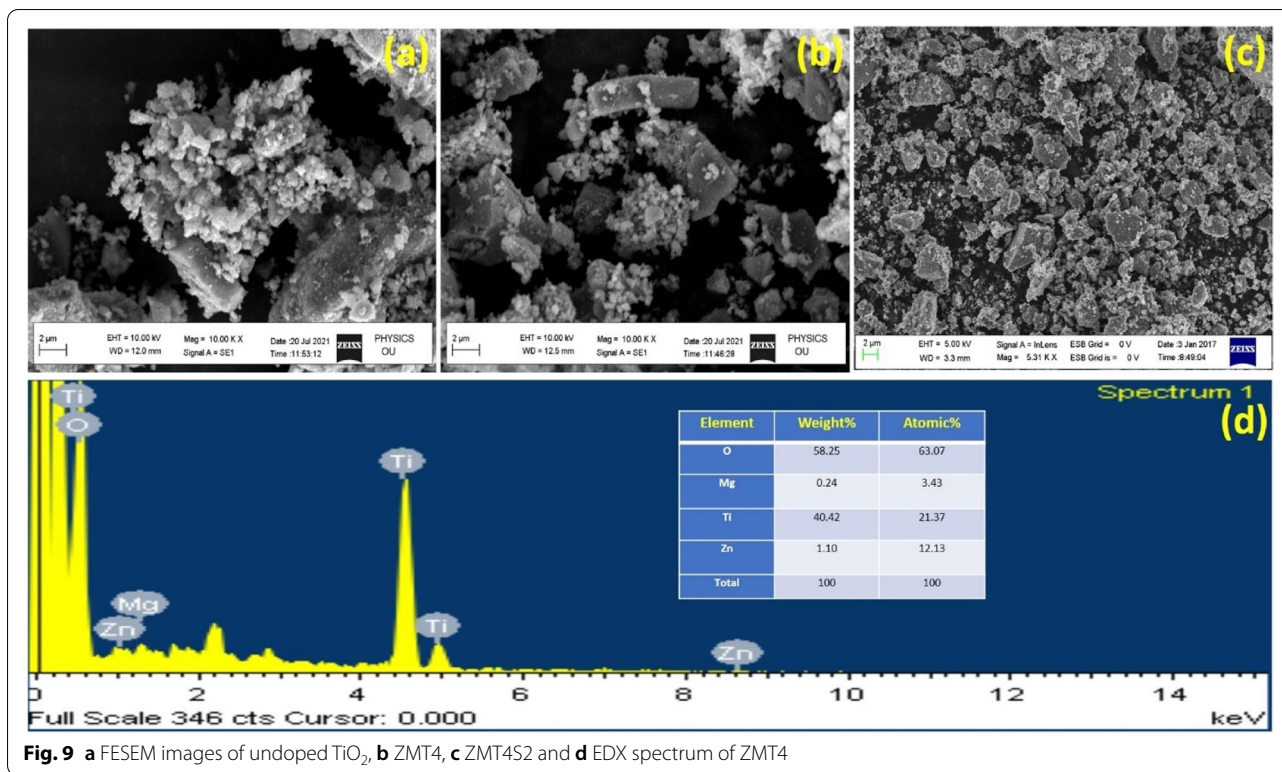


Fig. 9 a FESEM images of undoped TiO<sub>2</sub>, b ZMT4, c ZMT4S2 and d EDX spectrum of ZMT4

Table 5 XRF analysis of Zn/Mg co-doped TiO<sub>2</sub> for doped concentration in ZMT4

Element	wt (%)	Atomic (%)
Ti	98.8	98.7
Mg	0.22	0.23
Zn	1.14	1.07

stirred in the dark for 60 min and the aliquot taken was analyzed for absorbance at the same  $\lambda_{max}$ . A small change in absorbance of the dye was observed indicating the adsorption of dye molecules on the surface of the charged catalyst.

### 4.3 Photocatalysis

The reaction vessels containing above-said components were kept in visible light irradiation for 60 min under continuous stirring and at different time intervals the aliquots samples were taken and absorbance was measured. It is noted that the progressive decrease in absorbance

Table 6 Comparative crystallite size, bandgap, surface area, pore size and pore volume values of all synthesized catalysts

Nanomaterials	Crystallite size (nm)	Bandgap energy (eV)	BET surface analysis		
			Surface area (m <sup>2</sup> g <sup>-1</sup> )	Pore volume (cm <sup>3</sup> g <sup>-1</sup> )	Pore size (nm)
Undoped TiO <sub>2</sub>	32.5	3.2	74	0.12	48
ZMT1	8.0	2.9	114	0.21	57
ZMT2	7.9	2.8	122	0.22	60
ZMT3	7.5	2.8	124	0.20	61
ZMT4	7.0	2.7	132	0.23	63
ZMT5	8.2	3.0	86	0.14	52
ZMT4-S1	6.4	2.2	158	0.25	68
ZMT4-S2	5.7	2.1	195	0.29	87
ZMT4-S3	7.4	2.5	122	0.25	73

can be attributed to the interdependence of light and catalyst. The comparison of photolysis, adsorption, and photocatalysis is presented in Fig. 10. Based on the above-said conditions the reaction conditions have been optimized.

#### 4.4 Optimization of reaction conditions

To determine the influence of dopant concentrations on the efficiency of the catalyst, experiments were conducted at different dopant concentrations by keeping other parameters constant such as catalyst dosage  $0.05\text{ g }100\text{ mL}^{-1}$ , solution pH3, and initial dye concentration  $5\text{ mg L}^{-1}$ . The experimental results depicted in Fig. 11 reveal that the photocatalytic behavior of all the co-doped  $\text{TiO}_2$  catalysts (ZMT1-ZMT5) is more pronounced than undoped- $\text{TiO}_2$ , attributed to the narrowing of band gap as discussed in Sec. 3.5. But among all the catalysts, ZMT4 exhibits elevated rate of degradation which is ascribed to an utmost decrease in the bandgap of  $\text{TiO}_2$  in ZMT4 and reduction in electron/hole recombination. At higher concentrations of dopants, they deposit on the surface of the catalyst rather than substitution doping into  $\text{TiO}_2$  lattice. This can provoke the acceleration of electron/hole recombination which retards the rate of degradation [33]. Within these two dopants,  $\text{Mg}^{2+}$  formed an extra Fermi energy level by mixing of 2p orbitals of Mg and O. In the same way,  $\text{Zn}^{2+}$  facilitated an electron trap by forming an extra energy level below the conduction band by mixing of 3d orbitals of the conduction band and  $\text{Zn}^{2+}$  [9]. In view of the decrease in the band gap of catalyst particle, high quanta of visible radiations were absorbed leading to high quantum efficiency.

The ZMT4 data (1.00% Zn and 0.25% Mg) was found to be an effective photocatalyst and for further enhancement in the photocatalytic activity of ZMT4 two factors decrease in particle size and increase in surface area favour the enhancement process. To achieve this criterion, ZMT4 was re-synthesized in presence of biogenic surfactant at 3 different concentrations and the process was discussed in Sec. 2.2.2. After calcination the catalytic efficiency of these three catalysts (ZMT4S1, ZMT4S2 and, ZMT4S3) were evaluated and the results were shown in Fig. 12. Among these ZMT4S2 exerts highest photocatalytic activity than the other two because of the detrimental effect on further increasing the surfactant concentration causes the restriction for coherent doping of metal ions [34]. The rate degradation graph of these three catalysts is given in Fig. 12 as an inset. This result corroborated with the results obtained in XRD, TEM, and BET surface area analysis (Sec. 3.1, 3.2 and 3.4). During the further course of catalysis, ZMT4S2 was fixed as the best catalyst and other parameters were varied for obtaining optimum conditions.

The impact of solution pH on the photocatalytic activity of ZMT4S2 for the degradation of AB 10B dye was studied by varying the pH from 2 to 9 and keeping the other parameters constant such as catalyst dosage ( $0.05\text{ g }100\text{ mL}^{-1}$ ) and dye concentration ( $5\text{ mg L}^{-1}$ ). All the experimental results shown in Fig. 13 show that the degradation rate was observed to be high in acidic pH. Under acidic conditions  $<6.25$ , the surface hydroxyl group ( $\text{Ti-OH}$ ) undergoes protonation ( $\text{Ti-OH}_2^+$ ) by making the surface positive which facilitates the adsorption of negatively charged AB 10B dye molecule by electrostatic interaction. Further, increase in pH from 5 to 6, the positivity of the surface decreases slowly and becomes negative by approaching 8 to 9 pH. On the whole, pH3 is the better optimal condition where the surface of the catalyst is positive which is more favorable for the adsorption of negative dye molecule. Hence, at this condition, the rate of degradation is high. At pH2, the approachability of the  $\text{H}^+$  towards  $\text{Ti-OH}$  on the surface is more competitive due to repulsion between protons [28].

Figure 14 illustrates the photocatalytic activity of ZMT4S2 at different catalyst loading varying from  $0.05$  to  $0.20\text{ g }100\text{ mL}^{-1}$  keeping other parameters constant. It is observed that the catalyst dosage at  $0.1\text{ g }100\text{ mL}^{-1}$  exhibited the highest rate of degradation, later it decreases by increasing the catalyst dosage. This condition may be attributed to the greater availability of catalyst up to optimum concentration ( $100\text{ mg L}^{-1}$ ) beyond which the increase in catalyst concentration the degradation rate decreases due to non-availability of the sufficient dye molecules to react with the active catalyst particle, also high catalyst dosage concentration, increases the turbidity impeding the penetration of light henceforth lowering the photocatalytic efficiency in the given working conditions [35].

After selection of the catalyst, pH and, catalyst dosage, the final parameter initial dye concentration has to be optimized. Initial dye concentration varies from 5, 10, and  $15\text{ mg L}^{-1}$  by maintaining the other parameter constant. It can be inferred from the plot (Fig. 15a) that the rate of degradation increases up to  $10\text{ mg L}^{-1}$  dye concentration later it decreases ( $15\text{ mg L}^{-1}$ ), this is maybe attributed to that up to  $10\text{ mg L}^{-1}$  dye concentration, the surface area of photocatalyst is fully saturated with the monolayer adsorption and simultaneous degradation of dye molecule but at high concentration ( $15\text{ mg L}^{-1}$ ) due to blanket effect, multilayer adsorption of dye restricted the penetration of light to activate the surface of the catalyst [15]. Moreover, confinement of  $\cdot\text{OH}$  radicals at fixed catalyst dosage due to non-availability of catalyst particles confines the rate of degradation.

**Table 7** Comparison of photocatalytic degradation efficiency of Co-doped TiO<sub>2</sub> towards various dyes under visible light irradiation

Nanomaterials	Dye pollutant	% Degradation	Degradation time (min)	Ref.
Fe/Pr co-doped TiO <sub>2</sub>	Acid Orange 7	87	60	[37]
Zn/Br co-doped TiO <sub>2</sub>	Acid Red 6A	98	60	[6]
Mn/Mg co-doped TiO <sub>2</sub>	Methyl Red	99	60	[15]
Zn/Mg co-doped TiO <sub>2</sub>	Amido Black 10B	99	50	Present work
Zn/Mg co-doped TiO <sub>2</sub> (with surfactant)	Amido Black 10B	99	20	Present work

Further, the Langmuir-Hinshelwood (LH) model was used to confirm whether the solid-liquid interface was the site that dominated the heterogeneous photocatalytic degradation [36]. The L-H model was described as follows

$$\frac{1}{k} = \frac{C_0}{k_{LH}} + \frac{1}{k_{LH}k_L} \tag{1}$$

where *k* was the pseudo-first-order rate constant (min<sup>-1</sup>), *C*<sub>0</sub> was the initial concentration of AB 10B (mgL<sup>-1</sup>), *k*<sub>LH</sub> presents the L-H adsorption constant of AB 10B over ZMT4S2 surface (gL<sup>-1</sup>), and *k*<sub>L</sub> is the intrinsic reaction rate constant (mgmin<sup>-1</sup>). It could be extrapolated from the plot shown in (Fig. 15b), that the experimental data fit well with LH model (R<sup>2</sup>=0.997) implies the photocatalytic degradation of AB 10B primarily takes place at the surface of ZMT4S2 and there is a directly proportional linear relationship exists between 1/*k* and *C*<sub>0</sub>, which means that with an increase in initial AB 10B concentration could induce a decrease in *k* value. The value for *k*<sub>LH</sub> and *k*<sub>L</sub> can be calculated from the slope and intercept and were found to be 1.31 mg<sup>-1</sup>L and 0.63 L<sup>-1</sup>min<sup>-1</sup>, respectively.

Optimum conditions for efficient degradation (99%) of Amido Black 10B by ZMT4S2 was arrived at catalyst dosage (0.1 g 100 mL<sup>-1</sup>), dye concentration (10 mg L<sup>-1</sup>) maintained at pH 3.

The degradation efficiency of Zn/Mg co-doped TiO<sub>2</sub> was further checked and compared with previously reported works for dye degradation under visible light irradiation and has been presented in Table 7 [6, 15, 37].

**5 Identification of active species formed during photocatalysis using scavenger reagents**

To draw the reaction mechanism for photocatalytic degradation of AB 10B by using ZMT4S2, there is a need to identify the reaction species using scavenger reagents.

In the present research article, specific scavenging reagents were employed to identify the role of reactive

**Table 8** Specific scavenging reagents used for identification of reactive species

Reactive species	Scavenging Reagents
e <sup>-</sup> holes	EDTA
Superoxide radicals (O <sub>2</sub> <sup>-</sup> )	1,4 Benzoquinone
Hydroxyl radicals (•OH)	Coumarine

species such as e<sup>-</sup> holes, hydroxyl radicals (•OH), and superoxide radicals (•O<sub>2</sub><sup>-</sup>) as shown in Table 8.

**5.1 Assessing the role of e<sup>-</sup> holes and superoxide radicles**

For this purpose, the reaction medium consists of ZMT4S2 catalyst dosage (0.1g 100 mL<sup>-1</sup>), dye concentration (10 mgL<sup>-1</sup>) maintained at pH3 was taken in two separate beakers and carried out the reaction up to 5 min. Then in the first beaker an effective hole trap EDTA was added and the progress of the reaction was monitored. The decrease in the % degradation up to 25% is evident

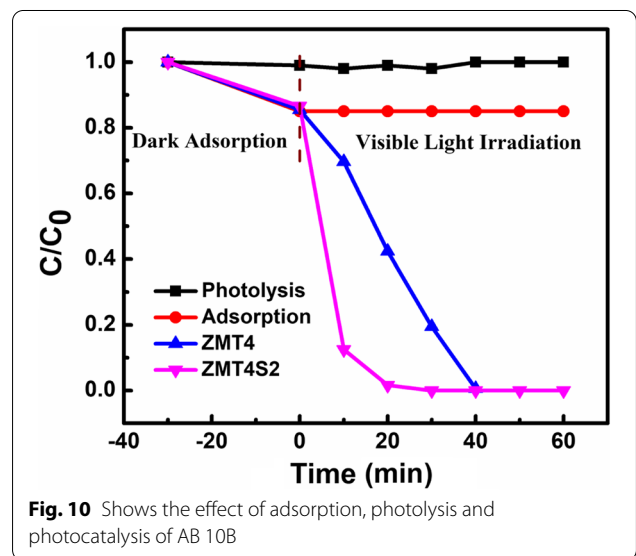


**Fig. 10** Shows the effect of adsorption, photolysis and photocatalysis of AB 10B

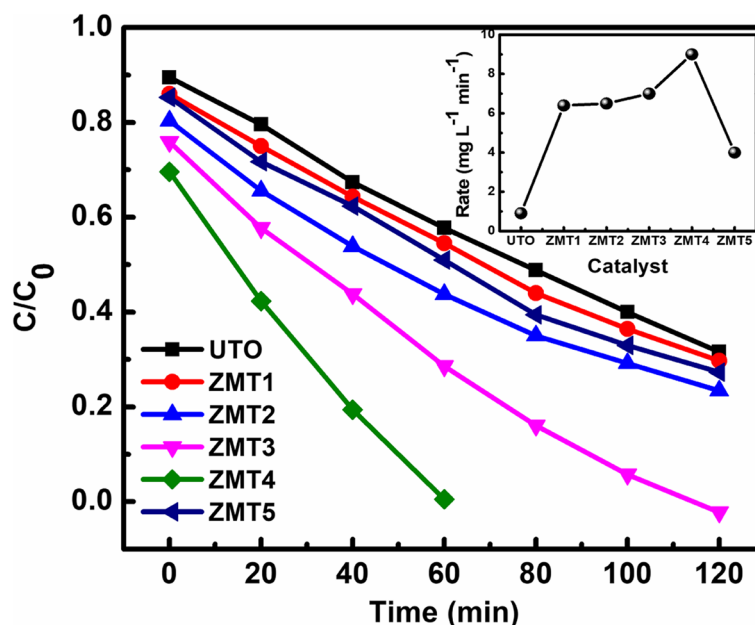


**Fig. 11** Shows the effect of dopant concentration on degradation of Amido Black 10B. (catalyst dosage  $0.05 \text{ g L}^{-1}$ , solution pH3, and initial dye concentration  $5 \text{ mg L}^{-1}$ )

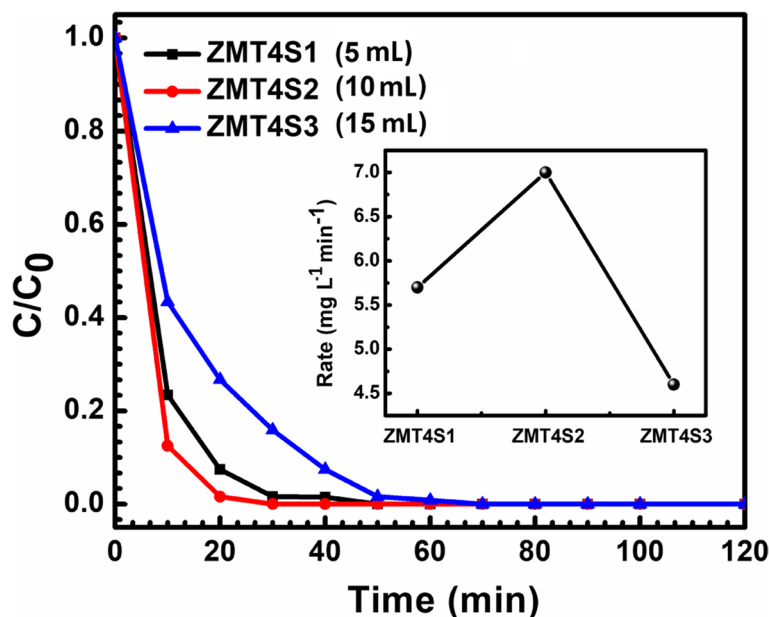


**Fig. 12** Shows the effect of surfactant concentration on degradation of Amido Black dye

for the suppression of the holes generated. This indicates the presence of photogenerated  $e^-$  holes in the reaction. In the second reaction vessel, the superoxide radical scavenger 1,4 Benzoquinone was added after 5 min of reaction. It resulted in the reduction of degradation up to 15% under given experimental conditions indicating the

formation of superoxide radical. The results are represented in Fig. 16 plot of % degradation v/s time.

### 5.2 Assessing the role of $\text{OH}^\bullet$ Radicle as reactive species

To investigate the production of  $\text{OH}^\bullet$  radicle as reactive species photoluminescence studies were conducted

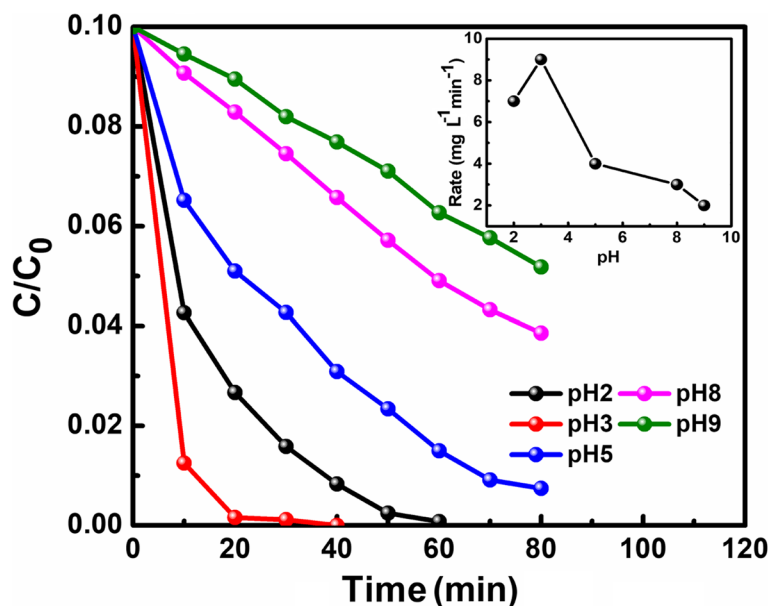


Fig. 13 Shows the impact of solution pH on the degradation of Amido Black 10 B dye

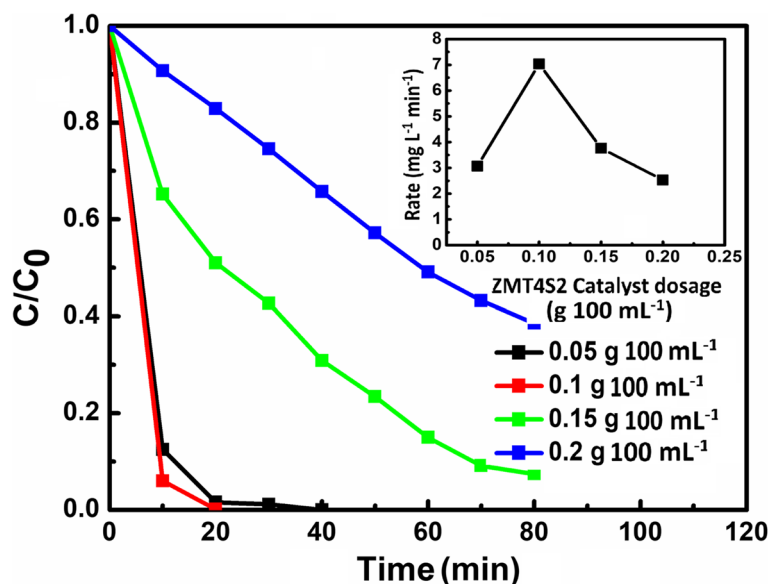


Fig. 14 Shows the impact of catalyst loading on degradation of AB 10 B

using coumarin as a probe molecule which after reaction with hydroxyl radical forms, highly fluorescent 7-hydroxy coumarin in the reaction medium, and the fluorescent intensity was measured at 450 nm. The corresponding obtained spectra was plotted Photoluminescence intensity against wavelength and the outcomes were presented in Fig. 17. It can be inferred from Fig. 17 that the produced  $\cdot\text{OH}$  was in proportionate to

the 7 hydroxy coumarin formed. The ZMT4S2 catalyst showed the presence of hydroxyl radical which after a course of irradiation decreases with time.

### 5.3 Detailed plausible mechanism for degradation of AB 10B using Zn/Mg co-doped TiO<sub>2</sub>

The mechanism for degradation of AB 10B using Zn/Mg co-doped TiO<sub>2</sub> has been explained below and given

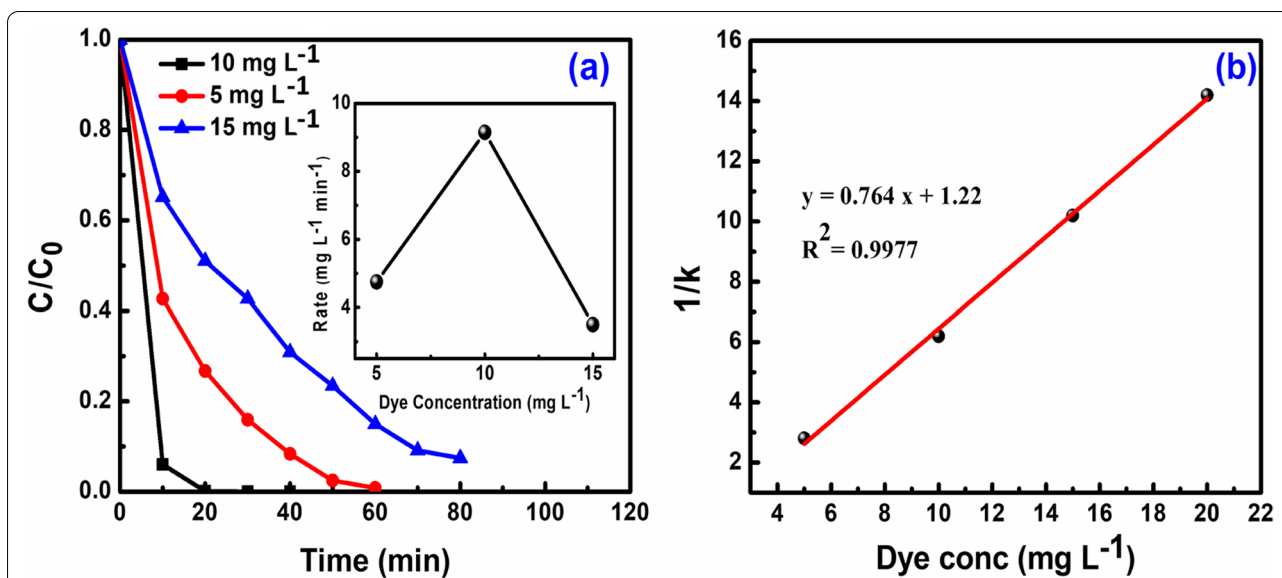


Fig. 15 a The effect of initial dye concentration on AB 10 B degradation. b LH model for AB 10B dye concentration

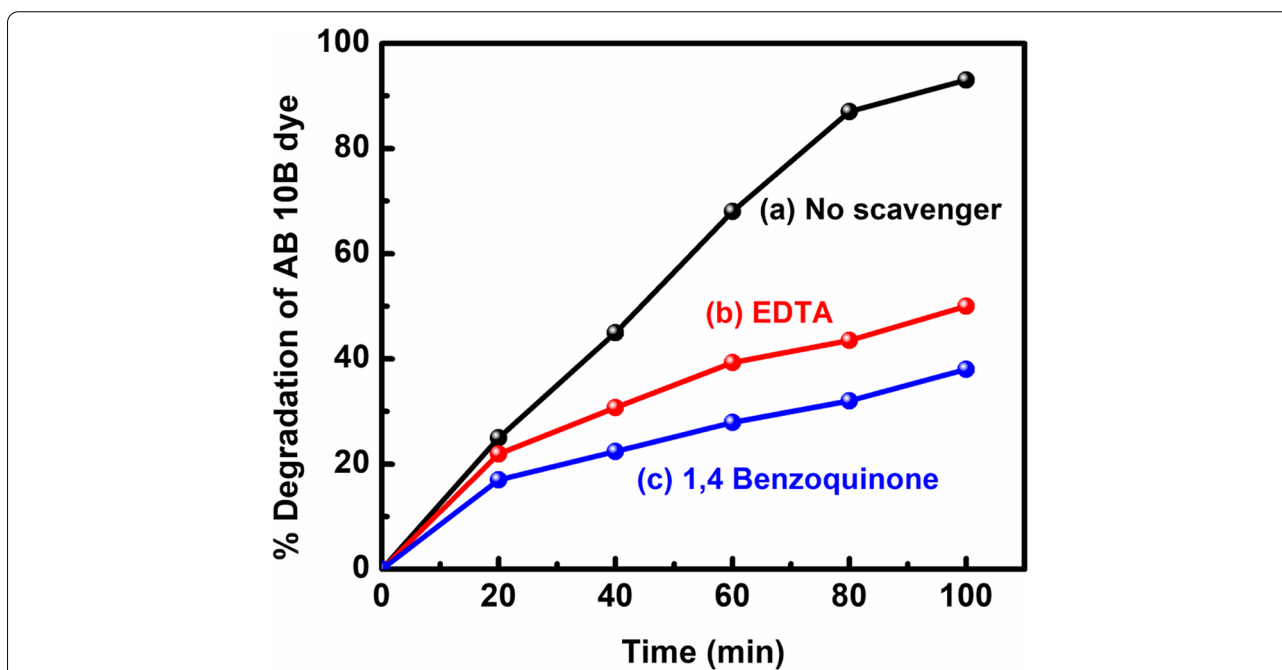
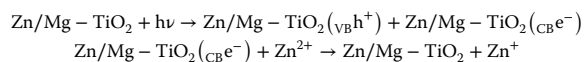
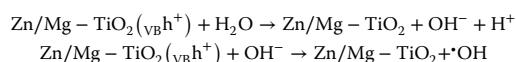


Fig. 16 Effect of e<sup>-</sup> hole and superoxide radicals (O<sub>2</sub><sup>-</sup>) scavenger on AB 10B degradation

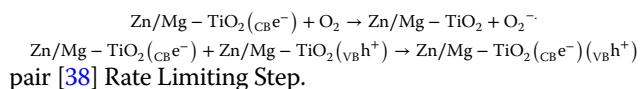
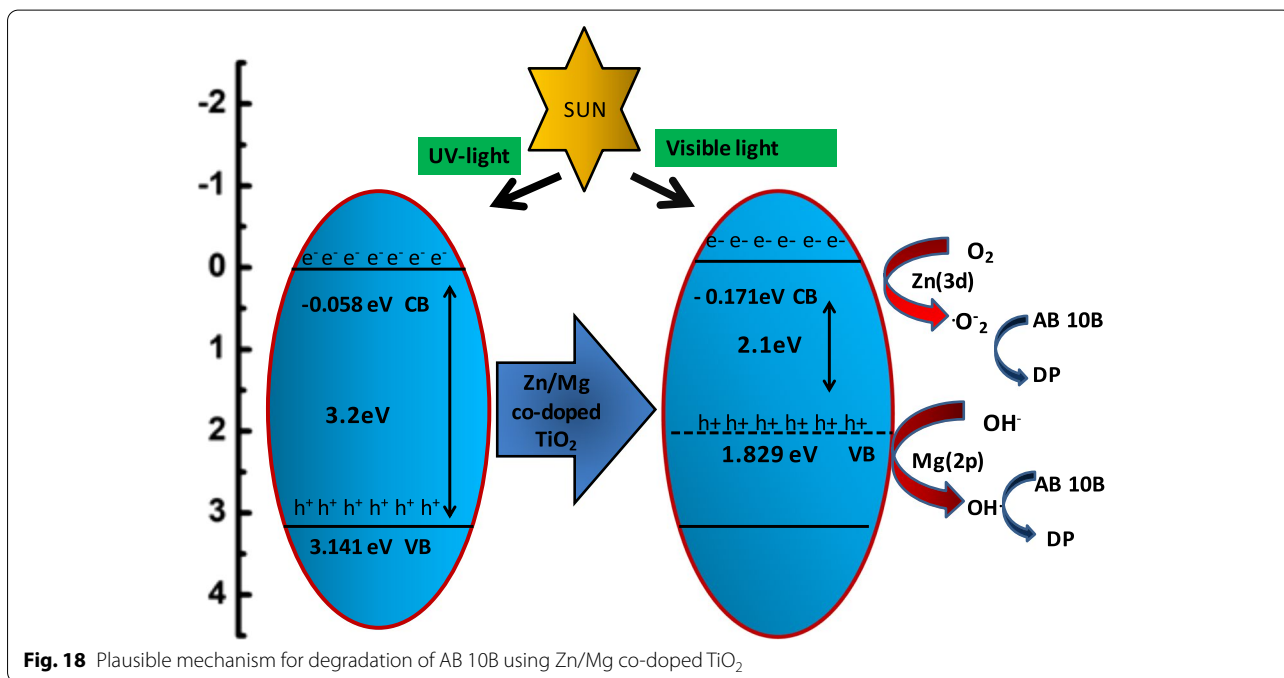
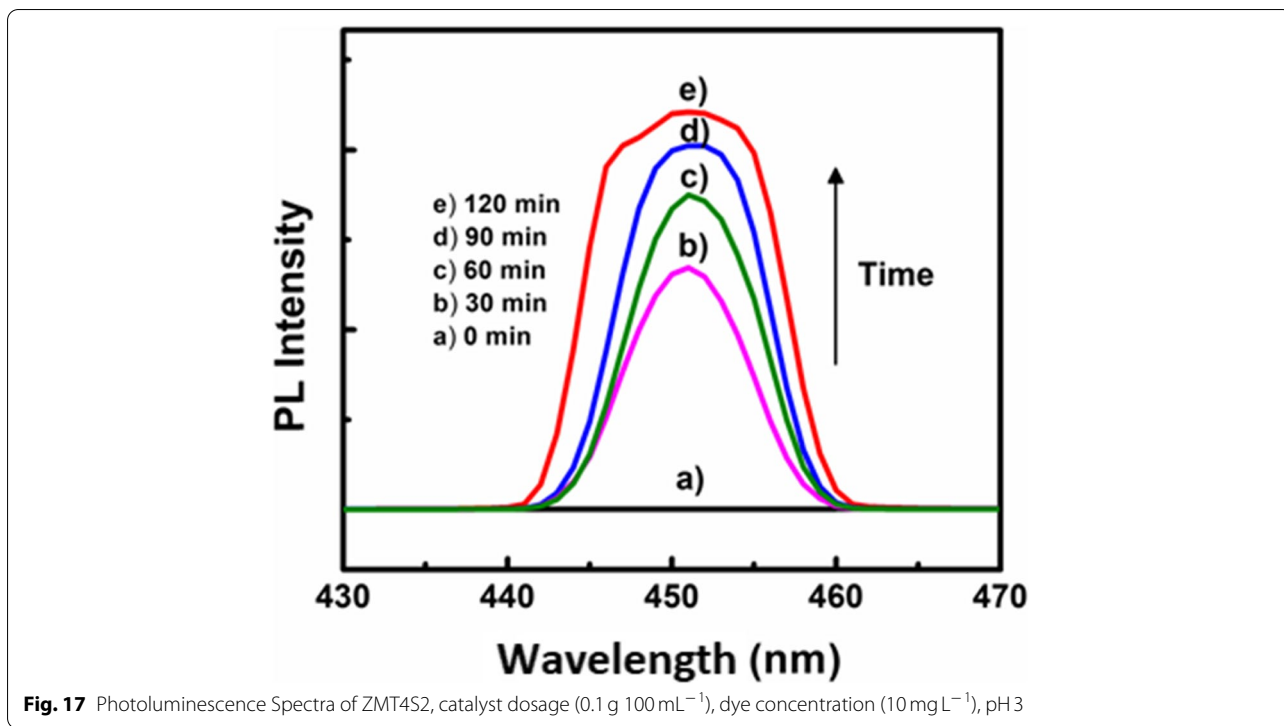
in Fig. 18. Irradiation of Zn/Mg-TiO<sub>2</sub> with visible light excites an e<sup>-</sup> from the valence band to the conduction band thus generating a hole on the valence band.



The holes thus generated reacts with the H<sub>2</sub>O or surface hydroxyl group to form hydroxyl radical and H<sup>+</sup>.



The excited electron on the conduction band reacts with the O<sub>2</sub> to produce superoxide radicals.



In our reaction, the rate-limiting step was avoided due to the presence of  $\text{Zn}^{2+}$  ion which acts as an electron trapper as discussed in Sec. 1.

The as-produced superoxide radical reacts with  $\text{H}_2\text{O}$  producing hydroperoxy radical and hydroxyl ion.

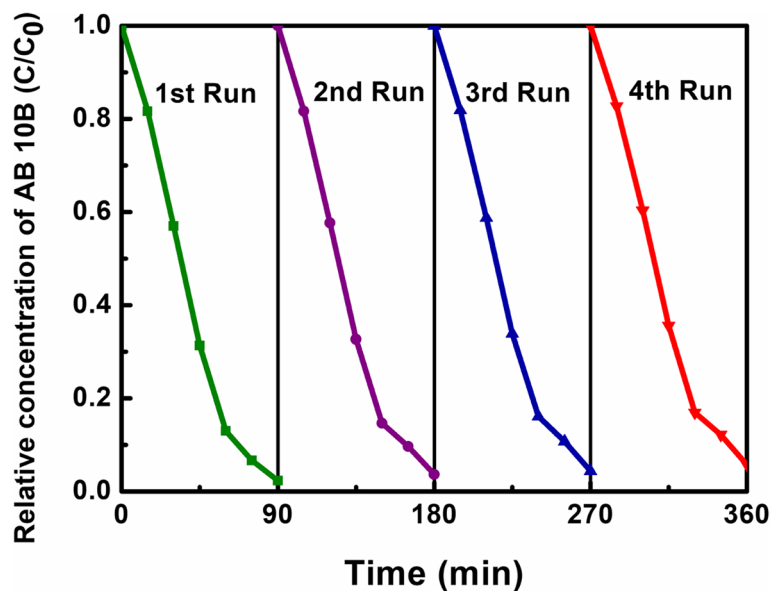
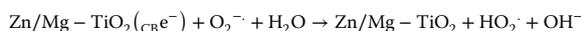
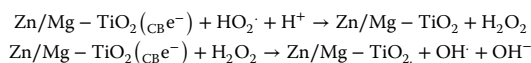


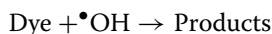
**Fig. 19** Recyclability test for ZMT4S2



The hydro peroxy radicals combine with  $\text{H}^+$  resulting in the formation of an intermediate product Hydrogen peroxide which in turn reacts with conduction band  $e^-$  to give hydroxyl radicals and hydroxyl ions.



The ultimate formation of hydroxyl and superoxide radicals acts as the main reactive species for the degradation of dye adsorbed on the surface of the catalyst.



## 6 Recyclability of ZMT4S2

In the present research scenario, both the stability and efficiency of a catalyst are prominent features to account for the quality of the catalyst. Based on this fact, our catalyst was active against AB 10B dye up to 4 successive cycles (Fig. 19) with a decrement of 3% in each cycle with no appreciable loss of photocatalytic activity even after 4 cycles. Later the activity of the catalyst tends to decrease appreciably with each cycle owing to the combination of factors including the substantial decrease in surface area and increase in rutile content when exposed to visible light or prolonged mechanical agitation. Also, rapid  $e^-$  hole recombination owing to the increase in charge carriers deteriorates the photocatalytic activity of the catalyst [39].

## 7 Conclusions

This paper offers a great insight into the green synthesis of Zn/Mg-codoped  $\text{TiO}_2$  assisted by capping agent, i.e., biogenic extract of *S. emerginatus* pericarp via sol-gel method. The complete strategical approach was designed to fully evaluate the potentiality of the synthesized visible light-driven Zn/Mg co-doped  $\text{TiO}_2$  for degradation of AB 10B dye. Among the as-synthesized catalysts, ZMT4 was found to be more efficient attributing to its polycrystalline rough spherical morphology with lattice planes coinciding with the XRD confirming the pure anatase form of catalysts. The photocatalytic performance of ZMT4 was further promoted by Biocapping with different surfactant concentrations (5, 10 and 15 mL). Amongst them ZMT4S2 (10 mL) showed the best results with respect to decreased band gap (2.10 eV) crystallite size (5.74 nm) and surface area ( $195 \text{ m}^2 \text{ g}^{-1}$ ). The TEM demonstrates the comparative particle size distribution of ZMT4 and ZMT4S2 without any agglomeration. The characterization results were further evident for the photodegradability of AB 10B which was achieved 99% within 20 min of visible light irradiation. The scavenger test results conclude the presence of  $e^-$  holes, superoxide radicals ( $\cdot\text{O}_2^-$ ), and hydroxyl radicals ( $\cdot\text{OH}$ ) as reactive species.

## Supplementary Information

The online version contains supplementary material available at <https://doi.org/10.1186/s42834-022-00149-4>.

Additional file 1.

### Acknowledgements

G. Jaishree is thankful to Andhra Pradesh Pollution Control Board (APPCB), Andhra Pradesh for providing fellowship during this work. [Lr.No.APPCB/RFS/UH3/2019].

### Authors' contributions

GJ: conceptualization, experimentation, data interpretation and writing-original draft; TSR: supervision and writing-original draft; IMR: data interpretation and assisted in original draft writing, editing and revisions; GD and M.L.V.P.C: writing-review & editing. All authors read and approved the final manuscript.

### Funding

Not Applicable.

### Availability of data and materials

All data generated or analyzed during this study are included in this published article.

### Declarations

### Competing interests

The authors declare that no competing interests

Received: 7 January 2022 Accepted: 14 August 2022

Published online: 03 September 2022

### References

- Zhang J, Xiao X, Nan J. Hydrothermal-hydrolysis synthesis and photocatalytic properties of nano-TiO<sub>2</sub> with an adjustable crystalline structure. *J Hazard Mater.* 2010;176:617–22.
- Thambiliyagodage C, Usgodaarachchi L. Photocatalytic activity of N, Fe and Cu co-doped TiO<sub>2</sub> nanoparticles under sunlight. *Curr Res Green Sustain Chem.* 2021;4:100186.
- Kubiak A, Bielan Z, Bartkowiak A, Gabala E, Piasecki A, Zalas M, et al. Synthesis of titanium dioxide via surfactant-assisted microwave method for photocatalytic and dye-sensitized solar cells applications. *Catalysts.* 2020;10:586.
- Zhuang H, Zhang Y, Chu Z, Long J, An X, Zhang H, et al. Synergy of metal and nonmetal dopants for visible-light photocatalysis: a case-study of Sn and Cu co-doped TiO<sub>2</sub>. *Phys Chem Chem Phys.* 2016;18:9636–44.
- Nasir M, Bagwasi S, Jiao Y, Chen F, Tian B, Zhang J. Characterization and activity of the Ce and N co-doped TiO<sub>2</sub> prepared through hydrothermal method. *Chem Eng J.* 2014;236:388–97.
- Mulpuri RK, Tirukkovalluri SR, Imandi MR, Alim SA, Kapuganti VDL. Zinc and boron co-doped nanotitania with enhanced photocatalytic degradation of Acid Red 6A under visible light irradiation. *Sustain Environ Res.* 2019;29:29.
- Aqeel M, Ikram M, Imran M, Ul-Hamid A, Kumar U, Shahbaz A, et al. TiO<sub>2</sub> Co-doped with Zr and Ag shows highly efficient visible light photocatalytic behavior suitable for treatment of polluted water. *RSC Adv.* 2020;10:42235–48.
- Bakhshayesh AM, Bakhshayesh N. Enhanced short circuit current density of dye-sensitized solar cells aided by Sr, V co-doped TiO<sub>2</sub> particles. *Mater Sci Semicond Process.* 2016;41:92–101.
- Jiang K, Zhang J, Luo R, Wan Y, Liu Z, Chen J. A facile synthesis of Zn-doped TiO<sub>2</sub> nanoparticles with highly exposed (001) facets for enhanced photocatalytic performance. *RSC Adv.* 2021;11:7627–32.
- Chen H, Zhu W, Zhang Z, Cai W, Zhou X. Er and Mg co-doped TiO<sub>2</sub> nanorod arrays and improvement of photovoltaic property in perovskite solar cell. *J Alloys Compd.* 2019;771:649–57.
- Wang J, Nie Y, Miao C, Tan Y, Wen M, Xiao W. Enhanced electrochemical properties of Ni-rich layered cathode materials via Mg<sup>2+</sup> and Ti<sup>4+</sup> co-doping for lithium-ion batteries. *J Colloid Interface Sci.* 2021;601:853–62.
- Olowoyo JO, Kumar M, Singhal N, Jain SL, Babalola JO, Vorontsov AV, et al. Engineering and modeling the effect of Mg doping in TiO<sub>2</sub> for enhanced photocatalytic reduction of CO<sub>2</sub> to fuels. *Catal Sci Technol.* 2018;8:3686–94.
- Rajaramanan T, Shanmugaratnam S, Gurunathanan V, Yohi S, Velauthapillai D, Ravirajan P, et al. Cost effective solvothermal method to synthesize Zn-Doped TiO<sub>2</sub> nanomaterials for photovoltaic and photocatalytic degradation applications. *Catalysts.* 2021;11:690.
- Meshesha DS, Matangi RC, Tirukkovalluri SR, Bojja S. Synthesis, characterization and visible light photocatalytic activity of Mg<sup>2+</sup> and Zr<sup>4+</sup> co-doped TiO<sub>2</sub> nanomaterial for degradation of methylene blue. *J Asian Ceram Soc.* 2017;5:136–43.
- Miditana SR, Tirukkovalluri SR, Raju IM, Alim SA, Jaishree G, Chippada ML V. Gemini surfactant assisted synthesis of mesoporous Mn/Mg bimetal doped TiO<sub>2</sub> nanomaterial: characterization and photocatalytic activity studies under visible light irradiation. *Sustain Environ Res.* 2021;31:6.
- Javed R, Zia M, Naz S, Aisida SO, Ao Q. Role of capping agents in the application of nanoparticles in biomedicine and environmental remediation: recent trends and future prospects. *J Nanobiotechnol.* 2020;18:1–15.
- Swarnavalli GCJ, Dinakaran S, Raman N, Jegadeesh R, Pereira C. Bio inspired synthesis of monodispersed silver nano particles using *Sapindus emarginatus* pericarp extract—Study of antibacterial efficacy. *J Saudi Chem Soc.* 2017;21:172–9.
- Balakrishnan S, Varughese S, Deshpande AP. Micellar characterization of saponin from *Sapindus mukorossi*. *Tenside Surfactant Deterg.* 2006;43:262–8.
- Donkadokula NY, Kola AK, Saroj D. Modelling and optimization studies on decolorization of brilliant green dye using integrated nanofiltration and photocatalysis. *Sustain Environ Res.* 2020;30:9.
- Gokakakar SD, Pavaskar PA, Salker A V. Photo-catalytic studies of Mn and Fe tetraphenyl porphyrins in the degradation of Amido Black 10B dye with solar light. *SN Appl Sci.* 2020;2:294.
- Damkale SR, Arbuji SS, Umarji GG, Rane SB, Kale BB. Highly crystalline anatase TiO<sub>2</sub> nanocuboids as an efficient photocatalyst for hydrogen generation. *RSC Adv.* 2021;11:7587–99.
- Abdelkhalek A, Al-Askar AA. Green synthesized ZnO nanoparticles mediated by *Mentha spicata* extract induce plant systemic resistance against Tobacco mosaic virus. *Appl Sci.* 2020;10:5054.
- El-Nahhal IM, Kodeh FS, Salem JK, Hamma T, Kuhn S, Hempelmann R, et al. Silica, mesoporous silica and its thiol functionalized silica coated MgO and Mg (OH)<sub>2</sub> materials. *Chem Africa.* 2019;2:267–76.
- Chandra MR, Reddy PSP, Rao TS, Pammi SVN, Kumar KS, Babu KV, et al. Enhanced visible-light photocatalysis and gas sensor properties of polythiophene supported tin doped titanium nanocomposite. *J Phys Chem Solids.* 2017;105:99–105.
- Seki T, Chiang K-Y, Yu C-C, Yu X, Okuno M, Hunger J, et al. The bending mode of water: A powerful probe for hydrogen bond structure of aqueous systems. *J Phys Chem Lett.* 2020;11:8459–69.
- Sowri Babu K, Ramachandra Reddy A, Sujatha C, Venugopal Reddy K, Mallika AN. Synthesis and optical characterization of porous ZnO. *J Adv Ceram.* 2013;2:260–5.
- Balakrishnan G, Velavan R, Batoo KM, Raslan EH. Microstructure, optical and photocatalytic properties of MgO nanoparticles. *Results Phys.* 2020;16:103013.
- Avasarala BK, Tirukkovalluri SR, Bojja S. Photocatalytic degradation of monocrotophos pesticide—an endocrine disruptor by magnesium doped titania. *J Hazard Mater.* 2011;186:1234–40.
- Prabhakar Rao N, Rao TS, Lakshmi KVD, Divya G, Jaishree G, Raju IM, et al. Enhanced photocatalytic performance of Nb doped TiO<sub>2</sub>/reduced graphene oxide nanocomposites over rhodamine B dye under visible light illumination. *Sustain Environ Res.* 2021;31:37.
- Rai S, Acharya-Siwakoti E, Kafle A, Devkota HP, Bhattarai A. Plant-derived saponins: a review of their surfactant properties and applications. *Sci.* 2021;3:44.
- Athira K, Merin KT, Raguram T, Rajni KS. Synthesis and characterization of Mg doped TiO<sub>2</sub> nanoparticles for photocatalytic applications. *Mater Today Proc.* 2020;33:2321–7.
- Bramhankar TS, Pawar SS, Shaikh JS, Gunge VC, Beedri NI, Baviskar PK, et al. Effect of Nickel–Zinc Co-doped TiO<sub>2</sub> blocking layer on performance of DSSCs. *J Alloys Compd.* 2020;817:152810.
- Etacheri V, Di Valentin C, Schneider J, Bahnemann D, Pillai SC. Visible-light activation of TiO<sub>2</sub> photocatalysts: advances in theory and experiments. *J Photochem Photobiol C: Photochem Rev.* 2015;25:1–29.
- Stroková V, Gubareva E, Ogurtsova Y, Fediuk R, Zhao P, Vatin N, et al. Obtaining and properties of a photocatalytic composite material of the “SiO<sub>2</sub>-TiO<sub>2</sub>” system based on various types of silica raw materials. *Nanomaterials.* 2021;11:866.

35. Nguyen AT, Juang R-S. Photocatalytic degradation of p-chlorophenol by hybrid H<sub>2</sub>O<sub>2</sub> and TiO<sub>2</sub> in aqueous suspensions under UV irradiation. *J Environ Manag.* 2015;147:271–7.
36. Wang F, Feng Y, Chen P, Wang Y, Su Y, Zhang Q, et al. Photocatalytic degradation of fluoroquinolone antibiotics using ordered mesoporous g-C<sub>3</sub>N<sub>4</sub> under simulated sunlight irradiation: kinetics, mechanism, and antibacterial activity elimination. *Appl Catal B Environ.* 2018;227:114–22.
37. Mancuso A, Sacco O, Vaiano V, Sannino D, Pragliola S, Venditto V, et al. Visible light active Fe-Pr co-doped TiO<sub>2</sub> for water pollutants degradation. *Catal Today.* 2021;380:93–104.
38. Wang CM, Heller A, Gerischer H. Palladium catalysis of O<sub>2</sub> reduction by electrons accumulated on TiO<sub>2</sub> particles during photoassisted oxidation of organic compounds. *J Am Chem Soc.* 1992;114:5230–4.
39. Sorathiya K, Mishra B, Kalarikkal A, Reddy KP, Gopinath CS, Khushalani D. Enhancement in rate of photocatalysis upon catalyst recycling. *Sci Rep.* 2016;6:1–9.

### Publisher's Note

Springer Nature remains neutral with regard to jurisdictional claims in published maps and institutional affiliations.

Ready to submit your research? Choose BMC and benefit from:

- fast, convenient online submission
- thorough peer review by experienced researchers in your field
- rapid publication on acceptance
- support for research data, including large and complex data types
- gold Open Access which fosters wider collaboration and increased citations
- maximum visibility for your research: over 100M website views per year

At BMC, research is always in progress.

Learn more [biomedcentral.com/submissions](https://biomedcentral.com/submissions)

